Pan Bowen (Orcid ID: 0000-0002-4617-5936)
Wang Yuan (Orcid ID: 0000-0001-6657-8401)
Logan Timothy (Orcid ID: 0000-0003-2648-1749)
Jiang Jonathan, H (Orcid ID: 0000-0002-5929-8951)

Determinant Role of Aerosols from Industrial Sources in Hurricane Harvey's Catastrophe

Bowen Pan[1,2], Yuan Wang[3,4], Timothy Logan[1], Jen-Shan Hsieh[1], Jonathan H. Jiang[4], Yixin Li[5], Renyi Zhang[1,5]

[1]Department of Atmospheric Sciences, Texas A&M University, College Station, TX, USA.
[2]Department of Atmospheric Science, Colorado State University, Fort Collins, CO, USA.
[3]Division of Geological and Planetary Sciences, California Institute of Technology, Pasadena, CA, USA.
[4]Jet Propulsion Laboratory, California Institute of Technology, Pasadena, CA, USA.
[5]Department of Chemistry, Texas A&M University, College Station, TX, USA.

Corresponding authors: Yuan Wang (yuan.wang@caltech.edu) and Renyi Zhang (renyi-zhang@geos.tamu.edu)

Key Points:

- Aerosol increases accumulative precipitation by a factor of 2-3 and invigorates lightning activities in Houston during Hurricane Harvey.
- Observations show intense lightning over Houston which exhibit geographic similarity to climatological maximum lightning flash.
- To better forecast extreme weather events, it is essential to account for aerosol effects in operational weather forecast models.

This article has been accepted for publication and undergone full peer review but has not been through the copyediting, typesetting, pagination and proofreading process which may lead to differences between this version and the Version of Record. Please cite this article as doi: 10.1029/2020GL090014

©2020 American Geophysical Union. All rights reserved.

Accepted Article

Plain Language Summary

The destructive power of tropical cyclones is due to the latent heat release from phase change of water, which is linked to airborne particles emitted from vehicle and petrochemical plants. The particles can act as cloud condensation nuclei and aid the formation of cloud droplets. The observation analyses reveal intense lightning and heavy precipitation in the proximity of Houston metropolitan region and these hotspots exhibit a striking geographic similarity to a decadal climatological maximum of lightning flash density in the south-central U.S. Moreover, the numerical model simulations show aerosol increases precipitation and invigorates lightning activities by a factor of 2-3 in the Houston region during Hurricane Harvey, unraveling the key factor in regulating flooding during this extreme weather event.

Abstract

The destructive power of tropical cyclones is driven by latent heat released from water condensation and is inevitably linked to the abundance of aerosols as cloud condensation nuclei. However, the aerosol effects are unaccounted for in most operational hurricane forecast models. We combined multi-source measurements and cloud-resolving model simulations to show fundamentally altered cloud microphysical and thermodynamic processes by anthropogenic aerosols during Hurricane Harvey. Our observations reveal intense lightning and precipitation in the proximity of Houston industrial areas, and these hotspots exhibit a striking geographic similarity to a decadal climatological maximum of lightning flash density in the south-central U.S. Our ensemble cloud-resolving simulations of Hurricane Harvey indicate that anthropogenic aerosols can increase precipitation and lightning by a factor of 2 in the Houston urban area, unraveling the key factor in regulating flooding during this weather extreme.

©2020 American Geophysical Union. All rights reserved.

1 Introduction

Hurricane Harvey wreaked havoc on southeast Texas with heavy rainfall of about 555 mm in the Houston urban area (29.5-30.0° N, 95.9-95.2° W) during 25-28 August 2017. As large and complex low-pressure systems associated with high surface enthalpy flux (Figure 1a), the development, intensity, and precipitation of tropical cyclones were regulated by several meteorological and environmental parameters, including sea surface temperature (SST), vertical wind shear, vorticity, and humidity of the free troposphere (Emanuel, 2017). Several studies have linked Hurricane Harvey's devastation to climate change (Emanuel, 2017; van Oldenborgh et al., 2017) or changes in land use due to urbanization (Zhang et al., 2018). In particular, human-caused climate changes have been implicated for increasing intensity and destruction of tropical cyclones in recent decades, by inducing favorable conditions (increasing SST) to supercharge hurricanes and increasing the risk of major damage (Emanuel, 2005, 2017; Goldenberg et al., 2001; Patricola and Wehner, 2018; Trenberth, 2005; van Oldenborgh et al., 2017). However, whether the characteristics of tropical cyclones have changed or will change under a warming climate remains controversial (Knutson et al., 2010). In addition, urbanization causes changes in land use, which were attributed to exacerbating the rainfall and flooding of Hurricane Harvey along the highly urbanized coastal Houston area (Zhang et al., 2018). Another key feature of tropical cyclones is reflected by efficient formation of hydrometeors and enormously large release of latent heat to fuel the destruction, i.e., storm surge, strong winds, and flooding. The amount of precipitation poured in the Houston urban area alone during this extreme event corresponds to an energy of about 5.5×10^{18} J estimated from water condensation. Currently, the relative contributions of the various factors to regulating the destructive power of tropical cyclones remain to be quantified.

From a microphysical perspective, the phase transformation of water molecules from vapor to liquid or ice is non-spontaneous and hindered by profound thermodynamic (free energy) and kinetic (curvature) barriers (Zhang et al., 2012), and the presence of aerosols is needed to act as cloud condensation nuclei (CCN) for cloud formation, precipitation, and storm development (Fan et al., 2018; Wang et al., 2011). There has been accumulating evidence that natural and anthropogenic aerosols play critical roles in cloud-related phenomena (Fan et al., 2018; Rosenfeld et al., 2008; Wang et al., 2011) as well as the genesis (Pan et al., 2018) and development (Herbener et al., 2014; Khain et al., 2008; Khain et al., 2010, 2016; Lynn et al., 2016; Rosenfeld et al., 2012; Wang et al., 2014a; Zhao et al., 2018) of tropical cyclones. However, most operational forecast (such as the Weather Research and Forecasting or WRF)

©2020 American Geophysical Union. All rights reserved.

models simulate the track and intensity of hurricanes using a prescribed number concentration of cloud droplets or a single moment microphysical scheme to represent the formation and growth of hydrometeors, which are insensitive to the aerosol effects (Zhang et al., 2018). Also, the number concentrations of CCN/cloud droplets in those models are typically fixed at a level characteristic of pristine maritime environments (Zhang et al., 2018) but significantly underrepresented over land, particularly in urban and industrial areas (Zhang et al., 2015).

As the country's fourth largest city, Houston hosts many industrial facilities, i.e., power plants, chemical manufactories, and petroleum refineries (Fan et al., 2005) (Figure 1b and Figure S1A). For example, the southeast Texas region (27-32° N and 94-98° W) is home to one of the world most densely distributed (over 400) refineries, which comprise approximately 40% of the nation's petrochemical capacity with a daily production of 0.3 million barrels. As evident from satellite measurements and emission estimations (Figure S2), the mass concentration of fine particulate matter (smaller than 2.5 μm or $PM_{2.5}$) in Houston often exceeds the annual average level of the National Ambient Air Quality Standards (Fan et al., 2005; Levy et al., 2013). Ground-based measurements and model simulations showed that elevated levels of aerosols emitted from industry considerably influence convection, lightning, and precipitation in this region (Fan et al., 2007; Hu et al., 2020; Li et al., 2008, 2009; Orville et al., 2001). A recent study by Souri et al. (2020) simulated a moderate increase in precipitation by aerosols over Houston, but the model baseline simulation was not fully evaluated by observational data. In this study, we combine ground-based rain gauge and radar measurements, high-density lightning detection network, as well as satellite storm and lightning observations to characterize Hurricane Harvey. Cloud-resolving model simulations of Hurricane Harvey are systematically compared with available measurements. The model sensitivity experiments with different aerosol emission scenarios shed light on the impacts of anthropogenic aerosols on Hurricane Harvey.

2 Materials and Methods

2.1 Observational Data

The observed rainfall data was taken from the hourly Stage IV Precipitation NCEP/EMC 4KM Gridded Data. The Stage IV precipitation analysis was based on a combination of surface rain gauge measurements and radar calculated rainfall produced by twelve River Forecast Centers (RFCs) in the Contiguous United States. Each RFC manually quality controls the Multisensor Precipitation Estimates (MPE) precipitation data in its

©2020 American Geophysical Union. All rights reserved.

respective region before being included in the national Stage IV mosaic. The hourly analyses were used in this work.

The lightning source points and lightning events data were from the Houston Lightning Mapping Array (HLMA), National Lightning Detection Network (NLDN), and Geostationary Lightning Mapper (GLM) on the Geostationary Operational Environmental Satellite (GOES-16). The HLMA is a three-dimensional total lightning location system that includes twelve lightning detection stations within 200 km of Houston, providing total lightning mapping for the Houston region and southeast Texas. Each station includes a Very High Frequency (VHF, 60 MHz) time-of-arrival total lightning mapping sensors built by New Mexico Institute of Mining and Technology (Cullen, 2013). The sensor detects the time of arrival of a VHF impulse emitted as part of the electrical breakdown and lightning propagation process. Data from each sensor are processed on a central LMA server to provide three-dimensional mapping of these impulses, i.e., LMA sources. The GLM, on board of the GOES-16, is a single-channel, near-infrared optical transient detector that can detect the momentary changes in an optical scene, indicating the presence of lightning. GLM measures the frequency, location and extent of lightning discharges, as well as total lightning activities (in-cloud, cloud-to-cloud and cloud-to-ground) with a near-uniform spatial resolution of approximately 10 km (GOES-R Algorithm Working Group and GOES-R Series Program, 2018). The NLDN consists of over 100 remote, ground-based sensing stations located across the U.S. that instantaneously detect the electromagnetic signals when lightning strikes occur (Orville et al., 2001). The spatial and temporal distributions of the LMA sources, NLDN strikes, and GLM level 2 lightning events were used in our analysis. The vertical cross-section and maximum radar reflectivity data were from the three-dimensional gridded Next Generation Weather Radar (NEXRAD; Bowman and Homeyer, 2017), i.e., the Weather Surveillance Radar, 1988, Doppler (WSR-88D) network.

2.2 Model Configuration and Experiment Design

The cloud-resolving Weather Research and Forecasting model version 3.6 (CR-WRF) was used for Hurricane Harvey simulations. The WRF model simulation was initialized at 0600 UTC 23 August 2017, and assimilated brightness temperature from the Geostationary Operational Environmental Satellite (GOES-16) were used from 0600 UTC 23 August to 0000 UTC 25 August. The free-run simulation covered the period from 0000 UTC 25 August to 0000 UTC 28 August with two two-way nested vortex-following domains and horizontal grid spacings of 27 km, 9 km, and 3 km (Figure S2A). The sea-surface temperature for the free-run was initiated from the Optimum Interpolated daily sea-surface temperature (Reynolds et al.,

©2020 American Geophysical Union. All rights reserved.

2007). For control and each sensitivity experiment, five ensemble simulations were performed, where the initial temperature field was randomly perturbed.

An aerosol-aware two-moment microphysics scheme was used in the CR-WRF simulations. A detailed description of this microphysical WRF framework has been described elsewhere (Li et al., 2008; Wang et al., 2014a). Briefly, the mass-mixing ratio and number concentration of aerosols were predicted. Aerosols activated as CCN according to the Kohler theory once the super-saturation criteria were reached (Li et al., 2008). The microphysical scheme calculated the mass-mixing ratios and number concentrations of five different types of hydrometeors, including cloud droplet, raindrop, ice crystal, snow, and graupel. Ice nucleation processes included deposition/condensation, immersion, contact, and homogeneous freezing. Supersaturation and droplet diffusional growth are explicitly calculated in the scheme.

Two scenarios, a clean (C-case) and a polluted case (P-case), were considered to realistically represent the concentration, emission, and distribution of natural and anthropogenic aerosols over the model domain. Aerosols in both cases consisted of anthropogenic aerosols and sea-spray aerosols (SSA). The initial concentrations of anthropogenic aerosols in the Houston urban area were 209 and 4192 cm^{-3} for the C- and P-cases, respectively, according to field measurements in the Houston urban area (Levy et al., 2013). These initial concentrations of anthropogenic aerosols in the Houston urban area, along with the aerosol optical depth (AOD) measured by the Moderate Resolution Imaging Spectroradiometer (MODIS) from 17 to 24 August, were used to derive the geographic distribution of anthropogenic aerosols inside the outer domain (8° S - 52° N, 13 – 118° W). Specifically, the initial concentrations of anthropogenic aerosols for the C- and P-cases at a grid-point over land were calculated by multiplying the aerosol concentrations in the Houston urban area for the two cases to the ratio of the values of the local to Houston AOD over the outer domain. The initial concentrations of anthropogenic aerosols over ocean were determined according to the same procedure, except that smaller aerosol concentrations (by ten times) were applied to the Houston values to reflect the land and ocean contrast. The SSA was uniformly distributed over land and ocean with the initial concentrations of 6 and 60 cm^{-3}, respectively. A sea salt production scheme was included, where SSA was produced according to the wind speed (Wang et al., 2014a). In addition, a constant emission rate of 46 kg s^{-1} was implemented to the bottom 1 km of the atmosphere in the Houston urban area to account for continuous emission of anthropogenic aerosols during Hurricane Harvey. Such an aerosol emission rate was close to half of that (105 kg s^{-1}) from the National Emission Inventory (U.S.

©2020 American Geophysical Union. All rights reserved.

Environmental Protection Agency, 2011) in the Houston urban area (Figure S2B). The SSA consisted of mainly sea salt with a hygroscopic parameter (κ) value of 0.9, and the anthropogenic aerosols had a κ value of 0.53, characteristic of the aerosol hygroscopicity measured in the Houston region (Levy et al., 2013). The removal of aerosols included activation to form cloud droplets, but precipitation scavenging was not considered in the present simulations. Advection of aerosols from the lateral boundaries into the model domain occurred under favorable wind conditions. The vertical distribution of SSA and anthropogenic aerosols followed an exponential decay, with the highest concentration at the surface.

4 Results

To assess the impacts of anthropogenic aerosols to precipitation and lightning during Hurricane Harvey, we analyzed ground- and satellite-based lightning (Figure 1, b-f, and Figure S1, B and C) and ground-based radar reflectivity (Figure 1, g-h) measurements. Highly intense lightning and radar reflectivity are evident in the southeast Texas region during 26-27 August. Measurements by the three-dimensional Houston Lightning Mapping Array (HLMA; Figure 1b), and satellite Geostationary Lightning Mapper (GLM; Figure S1B), and National Lightning Detection Network (NLDN; Figure S1C) exhibit a similar spatiotemporal pattern of unusually active lightning at the location surrounded by the Houston industrial facilities. A total of 0.23 million (both intracloud and cloud-ground) lightning flashes were detected by the NLDN from 26 to 28 August, and over 12 million lightning source points were recorded by HLMA during 26-27 August. Also, the lightning flashes exhibited large horizontal and vertical extensions. For example, an individual lightning strike with a horizontal dimension exceeding 40 km occurred on 27 August (Figure 1c). From 0510 to 0515 UTC 27 August, the most active lightning occurred at 29.4° N and 95.1° W (Figure 1d) and extended vertically from 5 to 15 km, with the maximum intensity at 10 km (Figure 1, e-f). The lightning hotspot (Figure 1d) collocated with the maximum radar reflectivity (Figure 1g). The vertical cross-section of radar reflectivity (Figure 1h) showed the maximum value of 50 dBZ reaching up to 10 km height, indicating strongest precipitation and convective activity. Evidently, the geographic distributions of the lightning hotspot detected by the GLM, HLMA and NLDN and the accumulative precipitation maximum (Figure 1b and Figure S1, B-D) during this event exhibit a striking similarity to a decadal climatological maximum lightning flash density in the south-central U.S. (Figure S1E; Orville et al., 2001).

Using a cloud-resolving WRF (CR-WRF) model, we quantified the aerosol effects on precipitation (Figure 2, a-d) and lightning (Figure 2, e-h) during Hurricane Harvey (Figure S3).

©2020 American Geophysical Union. All rights reserved.

Sensitivity simulations were performed under a clean (C) case to represent the pristine initial condition and a polluted (P) case to represent an elevated initial aerosol condition along with a continuous emission from the industrial sources (Figure S4). Specifically, our model simulations of the aerosol distributions, emissions, and properties were constrained by ground and satellite measurements in this region (Levy et al., 2013). Comparison between the C- and P-cases shows similar spatial distributions but distinct magnitude in precipitation. The accumulative precipitations during 26 and 28 August are much higher in the P-case than in the C-case (Figure 2, b-c), and the difference between the two cases ranges from 100 to 350 mm in the Houston urban area (Figure 2d). The distribution and magnitude of precipitation in the P-case are consistent with those from the observation (Figure 2a), while precipitation is significantly under-predicted in the C-case.

Based on the modeled hydrometeor contents, we calculated a lightning potential index (LPI) to reflect charge separation and cloud electrification (Wang et al., 2011; details are provide in SI). The LPI is highly elevated in the P- case but is minimal in the C-case (Figure 2, f-g), with the largest difference by a factor of 3 (Figure 2h). The spatial distribution of enhanced LPI in the P-case is also comparable to that of the lightning observation (Figure 2e).

The temporal evolution of the accumulative precipitation in the Houston urban area is comparable between the observation and P-case, with the values of 558 ± 47 mm and 600 mm, respectively, at 0000 UTC on 28 August (Figure 3a). In contrast, the accumulative precipitation (249 ± 19 mm) in the C-case is less than half of those of the observation and P-Case. The observed and simulated precipitation rates exhibit two intense periods (Figure 3b). The maximum precipitation rate (28 ± 5 mm hr^{-1}) in the P-case agrees with the observation (32 mm hr^{-1}), and both values are over a factor of 2 higher than that (11 ± 6 mm hr^{-1}) in the C-case. The temporal evolutions of the simulated LPI in the P- and C-cases are similar to the observation, while the LPI value is 2.8 times higher in the P-case than in the C-case (Figure 3c). The domain mean accumulated precipitation increase is about 29% (from ~138 mm to ~178 mm).

We analyzed the microphysical and thermodynamic characteristics relevant to hydrometeors and latent heating profiles in the simulations. The vertical cross-sections of mixing ratios of liquid and ice hydrometeors in the P-case are highly elevated between 2-4 km and 6-12 km, respectively, and large latent heat is released between 4-8 km (Figure S5, A, B, D, and E). The largest difference in the latent heating rates between the P- and C-cases is up to 10 K day^{-1} (Figure S5, C and F), corresponding to an increase of 250% in the P-case. The averaged vertical distributions of ice hydrometeor mixing ratios and latent heating rates in the Houston urban area show higher values of both quantities in the P-case than in the C-case

©2020 American Geophysical Union. All rights reserved.

during the two intense precipitation periods (Figure S6, A, B, G, and H). The maximum latent heating rate in the P-case is about two-fold higher than that in the C-case, because of more condensation in the warm regime. The average water (S_w) and ice (S_i) supersaturation at -13°C (or 7 km) over the Houston urban area are 0.16 and 0.03, respectively, in the P-case (Figure S7), indicating condensational/depositional growth of supercooled water/ice hydrometeors and continuous latent heat release in the mixed-phase regime. The higher S_w and S_i values below/at the freezing level in the P-case are attributed to a larger latent heat to yield a stronger buoyancy (Figure S6, A-D), which is augmented by strong cyclonic lifting (Figure 1, a-b) and abundant moisture supply (Figure S1D). The S_w and S_i values in the mixed-phase regime are higher in the C-case than in the P-case, because of lesser vapor depletion with fewer hydrometeors (Figure S7). Similarly, efficient condensation in the warm regime and elevated precipitation efficiency lead to the reduction of vapor mixing ratio between 2-4 km in the P-case (Figure S6, E and F). Condensation in the warm regime and condensation/deposition/riming in the mixed-phase regime are higher in the P-case, resulting in about 2 times larger latent heating rate and updraft velocity (Figure S6, C and D). Hence, the increases in liquid/ice contents, latent heating rate, and vertical velocity in the P-case result in localized enhancement of precipitation and lightning in the southeast Texas region (Figure 2 and 3).

Additional simulation was performed by implementing the continuous aerosol emission to the C-case (referred to as C-emis). This sensitivity experiment allows assessment of the impacts of continuous aerosol emissions during the storm, since many major industrial facilities in this region remained operational amid Hurricane Harvey. Comparison between the C-emis and C-case reveals a profound effect of continuous industrial emissions on precipitation (Figure S8). The spatial distribution of precipitation in C-emis (Figure S8 A and C) is similar to that of the observation (Figure 2a), and the difference in precipitation between the two cases reaches 200-300 mm over a large area downwind of the Houston industrial area (Figure S8C) and about 100 mm in the Houston urban area at 0000 UTC 28 August (Figure S8D). On the other hand, the total accumulated precipitation in C-emis is smaller than those of the P-case and observation (Figure 2c, Figure 3a, and Figure S8C), indicating that both the initial conditions and continuous emission of aerosol contribute to the flooding during Hurricane Harvey.

Our simulations well reproduce the track (defined by the minimum surface pressure) and intensity (defined by the minimum surface pressure and the maximum wind speed) during the storm evolution, especially considering the first landfall near Corpus Christi and stalling across inland Texas. The simulated track is insensitive to the aerosol perturbations (Figure 3d). A comparison of the minimum pressures and maximum wind speeds between the P-and C-

©2020 American Geophysical Union. All rights reserved.

cases shows a slightly lower surface pressure and higher wind speed, respectively, in the P-case during the intensification stage before 26 August (Figure 3, e-f), indicating an aerosol invigoration effect near the eyewall when CCN efficiently penetrates in. After the landfall, the aerosol effects on the track and intensity are minimal, in contrast with the common notion that elevated aerosols considerably impact the eyewall strength, development, and intensity of hurricanes (Rosenfeld et al., 2008; Wang et al., 2014b). One important reason is that there is an absence of the well-defined eyewall and symmetric rainband for Hurricane Harvey, but the presence of locally intensified precipitation, lightning, and radar reflectivity in the southeast Texas region. Our observations and simulations reveal inhomogeneous distribution and intensity in precipitation, lightning, and radar reflectivity (Figures 1-3).

The extreme precipitation and lightning during Hurricane Harvey are linked to anthropogenic aerosols from industrial emissions, which fundamentally alter the cloud microphysical and thermodynamic processes (Li et al., 2008; Orville et al., 2001; Rosenfeld et al., 2008; Wang et al., 2011). Elevated aerosols from the industrial sources act as CCN (Figure 4a) to produce more numerous and uniformly distributed but smaller cloud droplets in the warm regime (Figure S9). For warm rain processes (Figure 4b), precipitation formation in the warm regime includes condensation ($dr/dt \propto (1/r, S_w)$), and collision/coalescence growth ($dr/dt \propto r^2$) for cloud droplets, which are fast (slow) for small (large) sizes and are slow (fast) for small (large) sizes, respectively. Condensation growth of cloud droplets (~10-20 μm) to reach rain drops (~1 mm) is too slow at small S_w, and the formation of warm precipitation requires transition from condensation to collision/coalescence growth (black arrow). A higher concentration of cloud droplets results in a larger latent heat release and stronger buoyancy from vapor condensation (Figure S6, A-D), but a narrow distribution of cloud droplets with smaller sizes effectively inhibits collision/coalescence. In addition to buoyant and cyclonic lifting, a suppressed warm rain is essential to maintaining the updraft, since falling of raindrops would otherwise induce downdraft. In the absence of warm precipitation, cloud droplets are effectively transported above the freezing level. In the mixed-phase regime, precipitation formation includes vapor condensation/deposition to supercooled/ice (black arrow) and accretion of supercooled droplets by ice (riming). Deposition growth of ice is efficient in the mixed-phase regime because of high S_i, forming large snowflakes that further grow to large graupels by riming. The average S_i value of 0.16 in the P-case at 7 km is higher than that of 0.13 derived from the difference in the saturation vapor pressures between supercooled water and ice, indicating a minor role of deposition growth at the expense of supercooled droplets via

©2020 American Geophysical Union. All rights reserved.

the Bergeron process (blue arrow). The enhanced buoyancy and inhibited rain formation in the warm regime both facilitate vertical lifting and promote the mixed-phase processes, leading to efficient growth of ice hydrometeors by vapor deposition and riming in the P-case (Figure 4c). The combination of the increases in the contents of liquid/ice hydrometeors (Figure S5), latent heat release (Figure S6, A-B), and updraft velocity (Figure S6, C-D) from the C- to P-cases significantly modifies the hurricane characteristics (Figure 4).

The remarkable similarity in the geographic distributions between the extreme flooding/lightning during this event and the maximum lightning flash density from the decadal climatology in the south-central U.S. (Orville et al., 2001) is not a coincidence (Figure S1, B to C), and both are linked to elevated aerosols from industrial emissions in the Houston region (Levy et al., 2013). Another recent study also showed active warm rain near the eyewall in the early stage on 25 August and significant development of the mixed-phase cloud at the rainband on 26 August during Hurricane Harvey (Hu et al., 2020), consistent with our observational and modeling findings.

5 Conclusions

Our combined observational and modeling results unravel the microphysical and thermodynamic evidences to unambiguously establish anthropogenic aerosols as the major factor in regulating the energetics and flooding during Hurricane Harvey. Forecast made by the U.S. National Weather Service during this event exhibited major disparity from the observation (Figure S10), largely because of the inability of operational forecast models to account for the aerosol effects (Zhang et al., 2018). In addition, industrial sources likely produce ultrafine particles (Junkermann and Hacker, 2019; Zhang et al., 2012) to contribute to convection and rainfall enhancement, via an analogous invigoration mechanism (Fan et al., 2018). The effects of ultrafine particles on tropical cyclones can only be creditably assessed with measurements of their size distributions and number concentrations and clearly warrant future investigation. The determinant role of industrialization in causing heavy flooding during Hurricane Harvey underscores the importance of representing the aerosol effects in operational forecast and global climate models for hurricane preparedness. It is also imperative that regulatory emission measures are considered to minimize future catastrophic destruction of hurricanes along the highly industrialized coastal area of the Gulf of Mexico.

Accepted Article

©2020 American Geophysical Union. All rights reserved.

Acknowledgments and Data

We were grateful to M. Minamide for providing satellite data assimilated WRF runs and C. R. Homeyer for accessing the radar reflectivity data. Funding: B.P. was supported by a NASA graduate fellowship in Earth Science. Y.W. and J.H.J. acknowledged the support of the Jet Propulsion Laboratory, California Institute of Technology, under contract with NASA. Additional support was provided by the Welch A. Foundation (A-1417) and NSF AGS-1700727 grants. Gridded NEXRAD WSR-88D Radar Data, which can be accessed at http://gridrad.org/index.html. The Stage IV NCEP/EMC 4 km Gridded precipitation data can be downloaded at https://data.eol.ucar.edu/dataset/21.093. The National Emission Inventory data can be found at https://www.epa.gov/air-emissions-inventories/2011-national-emissions-inventory-nei-data. The power plants and petrochemical refineries information can be found at https://www.eia.gov/maps/layer_info-m.php. The GOES-R Series Global Lightning Mapper data is available at https://www.bou.class.noaa.gov/saa/products/. All the WRF model simulation output used for this research can be downloaded from the website at http://web.gps.caltech.edu/~yzw/share/Pan-2020-GRL-Harvey. The code of WRF model used in this study is available at https://www2.mmm.ucar.edu/wrf/users/downloads.html. We also acknowledge the computational support from Texas A&M High Performance Research Computing (HPRC) facility and appreciate Ping Luo from Texas A&M HPRC facility for her help on the model setup. All requests for materials in this paper should be addressed to Yuan Wang (yuan.wang@caltech.edu).

Author Contributions

Y.W. and R.Z. conceived and designed the research. B.P. and Y.W. performed the satellite data analysis. B.P. and Y.W. performed the model simulation. B.P. and T.L. performed analysis of ground-based lightning and radar measurements. B.P., Y.W., J.H.S., J.H.J., and R.Z. analyzed the model results. B.P., Y.W., and R.Z. wrote the manuscript.

Accepted Article

©2020 American Geophysical Union. All rights reserved.

References

Aligo, E. A., B. Ferrier, & J. R. Carley (2018). Modified NAM Microphysics for Forecasts of Deep Convective Storms. *Mon. Wea. Rev., 146*, 4115–4153. https://doi.org/10.1175/MWR-D-17-0277.1.

Bowman, K., & Homeyer, C. R. (2017). GridRad - Three-Dimensional Gridded NEXRAD WSR-88D Radar Data. *Research Data Archive at the National Center for Atmospheric Research, Computational and Information Systems Laboratory.* https://doi.org/10.5065/D6NK3CR7. Accessed 28 May 2019.

Cullen, M. (2013). The Houston Lightning Mapping Array: Network Installation and Preliminary Analysis. *Master's thesis, Texas A & M University.* Available electronically from http://hdl.handle.net/1969.1/151109.

Emanuel, K. (2005). Increasing destructiveness of tropical cyclones over the past 30 years. *Nature, 436*(7051), 686-688. doi:10.1038/nature03906

Emanuel, K. (2017). Assessing the present and future probability of Hurricane Harvey's rainfall. *Proc Natl Acad Sci U S A, 114*(48), 12681-12684. doi:10.1073/pnas.1716222114

Fan, J., Rosenfeld, D., Zhang, Y., Giangrande, S. E., Li, Z., Machado, L. A. T., . . . de Souza, R. A. F. (2018). Substantial convection and precipitation enhancements by ultrafine aerosol particles. *Science, 359*(6374), 411-418. doi:10.1126/science.aan8461

Fan, J., Zhang, R., Li, G., Nielsen-Gammon, J., & Li, Z. (2005). Simulations of fine particulate matter (PM2.5) in Houston, Texas. *Journal of Geophysical Research: Atmospheres, 110*(D16). doi:10.1029/2005jd005805

Fan, J. W., Zhang, R. Y., Li, G. H., & Tao, W. K. (2007). Effects of aerosols and relative humidity on cumulus clouds. *Journal of Geophysical Research-Atmospheres, 112*(D14). doi:10.1029/2006jd008136

GOES-R Algorithm Working Group and GOES-R Series Program (2018): NOAA GOES-R Series Geostationary Lightning Mapper (GLM) Level 2 Lightning Detection: Events, Groups, and Flashes. [GLM-L2-LCFA]. *NOAA National Centers for Environmental Information*. doi:10.7289/V5KH0KK6. Accessed 28 May (2019).

Goldenberg, S. B., Landsea, C. W., Mestas-Nuñez, A. M., & Gray, W. M. (2001). The Recent Increase in Atlantic Hurricane Activity: Causes and Implications. *Science, 293*(5529), 474-479. doi:10.1126/science.1060040

Herbener, S. R., van den Heever, S. C., Carrio, G. G., Saleeby, S. M., & Cotton, W. R. (2014). Aerosol Indirect Effects on Idealized Tropical Cyclone Dynamics. *Journal of the Atmospheric Sciences, 71*(6), 2040-2055. doi:10.1175/Jas-D-13-0202.1

Hong, S.-Y. & Lim, J.-O. J. (2006). The WRF single-moment 6-class microphysics scheme (WSM6). *J. Korean Meteor. Soc.*, 42, 129–151.

Hong, S.-Y., Noh, Y., & Dudhia, J. (2006). A New Vertical Diffusion Package with an Explicit Treatment of Entrainment Processes. *Monthly Weather Review, 134*(9), 2318-2341. doi:10.1175/mwr3199.1

Hu, J., Rosenfeld, D., Ryzhkov, A., & Zhang, P. (2020). Synergetic Use of the WSR-88D Radars, GOES-R Satellites, and Lightning Networks to Study Microphysical Characteristics of Hurricanes. *Journal of Applied Meteorology and Climatology, 59*(6), 1051-1068. doi:10.1175/jamc-d-19-0122.1

Iacono, M. J., Delamere, J. S., Mlawer, E. J., Shephard, M. W., Clough, S. A., & Collins, W. D. (2008). Radiative forcing by long-lived greenhouse gases: Calculations with the AER radiative transfer models. *Journal of Geophysical Research-Atmospheres, 113*(D13). doi:10.1029/2008jd009944

©2020 American Geophysical Union. All rights reserved.

Junkermann, W., & Hacker, J. M. (2019). Ultrafine Particles in the Lower Troposphere: Major Sources, Invisible Plumes, and Meteorological Transport Processes. *Bulletin of the American Meteorological Society, 99*(12), 2587-2602. doi:10.1175/bams-d-18-0075.1

Kain, J. S. (2004). The Kain–Fritsch Convective Parameterization: An Update. *Journal of Applied Meteorology, 43*(1), 170-181. doi:10.1175/1520-0450(2004)043<0170:Tkcpau>2.0.Co;2

Khain, A., Cohen, N., Lynn, B., & Pokrovsky, A. (2008). Possible Aerosol Effects on Lightning Activity and Structure of Hurricanes. *Journal of the Atmospheric Sciences, 65*(12), 3652-3677. doi:10.1175/2008jas2678.1

Khain, A., Lynn, B., & Dudhia, J. (2010). Aerosol Effects on Intensity of Landfalling Hurricanes as Seen from Simulations with the WRF Model with Spectral Bin Microphysics. *Journal of the Atmospheric Sciences, 67*(2), 365-384. doi:10.1175/2009jas3210.1

Khain, A., Lynn, B., & Shpund, J. (2016). High resolution WRF simulations of Hurricane Irene: Sensitivity to aerosols and choice of microphysical schemes. *Atmospheric Research, 167*, 129-145. doi:10.1016/j.atmosres.2015.07.014

Knutson, T. R., McBride, J. L., Chan, J., Emanuel, K., Holland, G., Landsea, C., . . . Sugi, M. (2010). Tropical cyclones and climate change. *Nature Geoscience, 3*, 157. doi:10.1038/ngeo779

Levy, M. E., Zhang, R., Khalizov, A. F., Zheng, J., Collins, D. R., Glen, C. R., . . . Olaguer, E. (2013). Measurements of submicron aerosols in Houston, Texas during the 2009 SHARP field campaign. *Journal of Geophysical Research: Atmospheres, 118*(18), 10,518-510,534. doi:10.1002/jgrd.50785

Li, G., Wang, Y., Lee, K.-H., Diao, Y., & Zhang, R. (2009). Impacts of aerosols on the development and precipitation of a mesoscale squall line. *Journal of Geophysical Research, 114*(D17). doi:10.1029/2008jd011581

Li, G., Wang, Y., & Zhang, R. (2008). Implementation of a two-moment bulk microphysics scheme to the WRF model to investigate aerosol-cloud interaction. *Journal of Geophysical Research, 113*(D15). doi:10.1029/2007jd009361

Lin, Y. (2011) GCIP/EOP surface: Precipitation NCEP/EMC 4KM gridded data (GRIB) stage IV data. Version 1.0. doi:10.5065/d6pg1qdd. Accessed 29 may (2019)

Lynn, B. H., Khain, A. P., Bao, J. W., Michelson, S. A., Yuan, T., Kelman, G., . . . Benmoshe, N. (2016). The Sensitivity of Hurricane Irene to Aerosols and Ocean Coupling: Simulations with WRF Spectral Bin Microphysics. *Journal of the Atmospheric Sciences, 73*(2), 467-486. doi:10.1175/JAS-D-14-0150.1

Orville, R. E., Huffines, G., Nielsen-Gammon, J., Zhang, R. Y., Ely, B., Steiger, S., . . . Read, W. (2001). Enhancement of cloud-to-ground lightning over Houston, Texas. *Geophysical Research Letters, 28*(13), 2597-2600. doi:10.1029/2001gl012990

Pan, B., Wang, Y., Hu, J., Lin, Y., Hsieh, J.-S., Logan, T., . . . Zhang, R. (2018). Impacts of Saharan Dust on Atlantic Regional Climate and Implications for Tropical Cyclones. *Journal of Climate, 31*(18), 7621-7644. doi:10.1175/jcli-d-16-0776.1

Patricola, C. M., & Wehner, M. F. (2018). Anthropogenic influences on major tropical cyclone events. *Nature, 563*(7731), 339-346. doi:10.1038/s41586-018-0673-2

Reynolds, R. W., T. M. Smith, C. Liu, D. B. Chelton, K. S. Casey, and M. G. Schlax (2007). Daily High-Resolution-Blended Analyses for Sea Surface Temperature. *J. Climate, 20,* 5473–5496, doi:10.1175/2007JCLI1824.1.

Rosenfeld, D., Lohmann, U., Raga, G. B., O'Dowd, C. D., Kulmala, M., Fuzzi, S., . . . Andreae, M. O. (2008). Flood or Drought: How Do Aerosols Affect Precipitation? *Science, 321*(5894), 1309-1313. doi:10.1126/science.1160606

©2020 American Geophysical Union. All rights reserved.

Rosenfeld, D., Woodley, W. L., Khain, A., Cotton, W. R., Carrio, G., Ginis, I., & Golden, J. H. (2012). Aerosol Effects on Microstructure and Intensity of Tropical Cyclones. *Bulletin of the American Meteorological Society, 93*(7), 987-1001. doi:10.1175/Bams-D-11-00147.1

Souri, Amir H., Yunsoo Choi, John K. Kodros, Jia Jung, Jacob Shpund, Jeffrey R. Pierce, Barry H. Lynn, Alexander Khain, and Kelly Chance. (2020). Response of Hurricane Harvey's Rainfall to Anthropogenic Aerosols: A Sensitivity Study Based on Spectral Bin Microphysics with Simulated Aerosols. *Atmospheric Research* 242:104965.

Trenberth, K. (2005). Uncertainty in Hurricanes and Global Warming. *Science, 308*(5729), 1753-1754. doi:10.1126/science.1112551

U.S. Environmental Protection Agency (2011) *National Emissions Inventory, version 2 (Technical Support Document)*.

van Oldenborgh, G. J., van der Wiel, K., Sebastian, A., Singh, R., Arrighi, J., Otto, F., . . . Cullen, H. (2017). Attribution of extreme rainfall from Hurricane Harvey, August 2017. *Environmental Research Letters, 12*(12). doi:10.1088/1748-9326/aa9ef2

Wang, Y., Lee, K.-H., Lin, Y., Levy, M., & Zhang, R. (2014a). Distinct effects of anthropogenic aerosols on tropical cyclones. *Nature Clim. Change, 4*(5), 368-373. doi:10.1038/nclimate2144

Wang, Y., Lee, K.-H., Lin, Y., Levy, M., & Zhang, R. (2014b). Distinct effects of anthropogenic aerosols on tropical cyclones. *Nature Climate Change, 4*(5), 368-373. doi:10.1038/nclimate2144

Wang, Y., Wan, Q., Meng, W., Liao, F., Tan, H., & Zhang, R. (2011). Long-term impacts of aerosols on precipitation and lightning over the Pearl River Delta megacity area in China. *Atmospheric Chemistry and Physics, 11*(23), 12421-12436. doi:10.5194/acp-11-12421-2011

Weather Prediction Center, *Quantitative Precipitation Forecast Archive*. Retrieved from: https://www.wpc.ncep.noaa.gov/archives/qpf/get_qpf_images.php, accessed May 28 (2019).

Zhang, R., Khalizov, A. F., Wang, L., Hu, M., & Xu, W. (2012). Nucleation and Growth of Nanoparticles in the Atmosphere. *Chemical Reviews, 112*(3), 1957-2011. doi:10.1021/cr2001756

Zhang, R., Wang, G., Guo, S., Zamora, M. L., Ying, Q., Lin, Y., . . . Wang, Y. (2015). Formation of urban fine particulate matter. *Chemical Reviews, 115*(10), 3803-3855. doi:10.1021/acs.chemrev.5b00067

Zhang, W., Villarini, G., Vecchi, G. A., & Smith, J. A. (2018). Urbanization exacerbated the rainfall and flooding caused by hurricane Harvey in Houston. *Nature, 563*(7731), 384-388. doi:10.1038/s41586-018-0676-z

Zhao, C., Lin, Y., Wu, F., Wang, Y., Li, Z., Rosenfeld, D., & Wang, Y. (2018). Enlarging Rainfall Area of Tropical Cyclones by Atmospheric Aerosols. *Geophysical Research Letters, 45*(16), 8604-8611. doi:doi:10.1029/2018GL079427

Accepted Article

©2020 American Geophysical Union. All rights reserved.

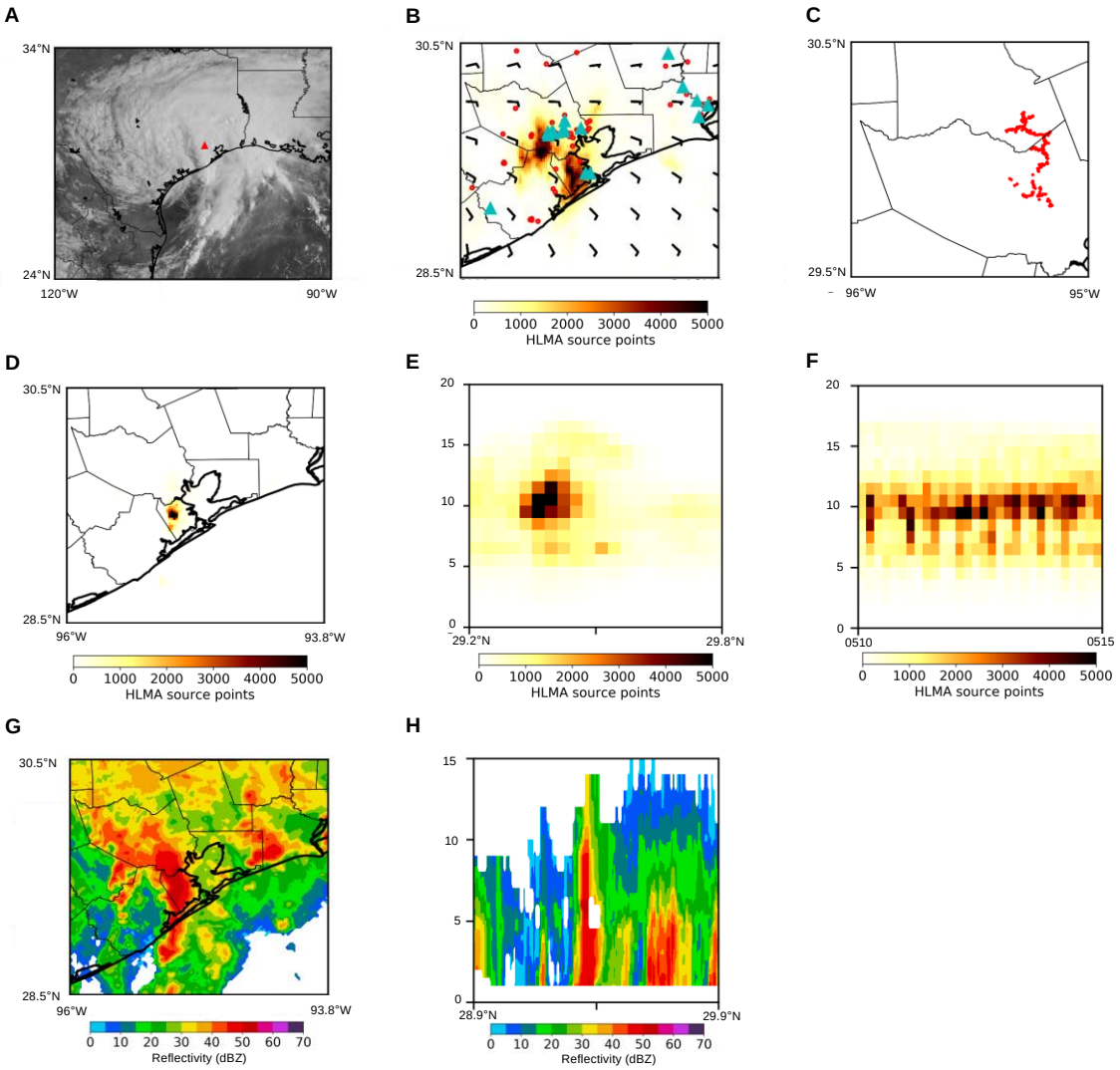

Figure 1. Intense lightning and precipitation in the Houston industrial proximity. (a) GOES-16 visible satellite image at 1504 UTC 27 August. The red triangle labels the location for the city of Houston. (b) Lightning distribution from HLMA on 27 August, which is overlaid with petroleum refineries (cyan triangles), power plants (red circles), and wind direction (black barbs). (c) A large lightning flash at 0300 UTC 27 August detected by HLMA. (d to h) An active storm episode at 0510-0515 UTC 27 August: horizontal distribution of HLMA source points (d), vertical zonal cross-section of HLMA source points (e), vertical time series of HLMA source points (f), base radar reflectivity in dBZ (g), and vertical cross-section of radar reflectivity in dBZ (h).

©2020 American Geophysical Union. All rights reserved.

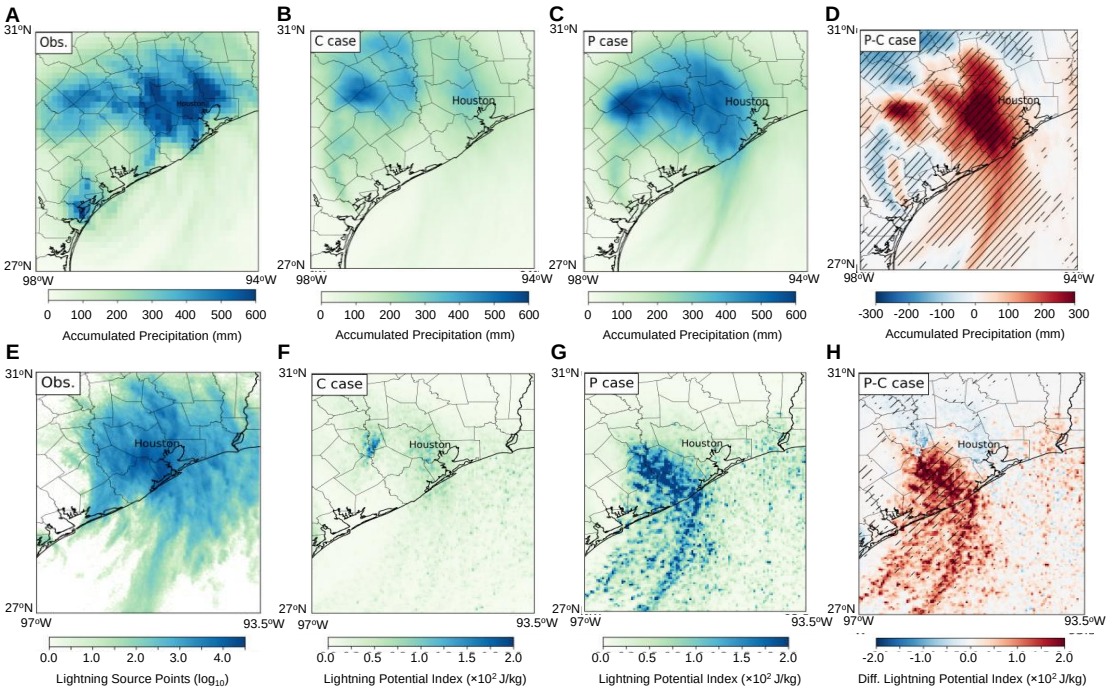

Figure 2. Aerosol-enhanced cyclonic precipitation and lightning. (a to d) Observed and simulated accumulative precipitation (mm) from 0000 UTC 26 August to 0000 UTC 28 August: observation from the NCEP Stage IV data (a), P-case (b), C-case (c), and the difference between P and C cases (d). (e) GOES-16 GLM lightning events from 0000 UTC 26 August to 0000 UTC 28 August. (f to h) Simulated LPI from 0000 UTC 26 August to 2330 UTC 27 August: P-case (f), C-case (g), and the difference between the P- and C-cases (h). Hatched lines denote the significant difference between the P- and C-cases according to the Student's t-test at the 95% confidence level.

Accepted

©2020 American Geophysical Union. All rights reserved.

Accepted Article

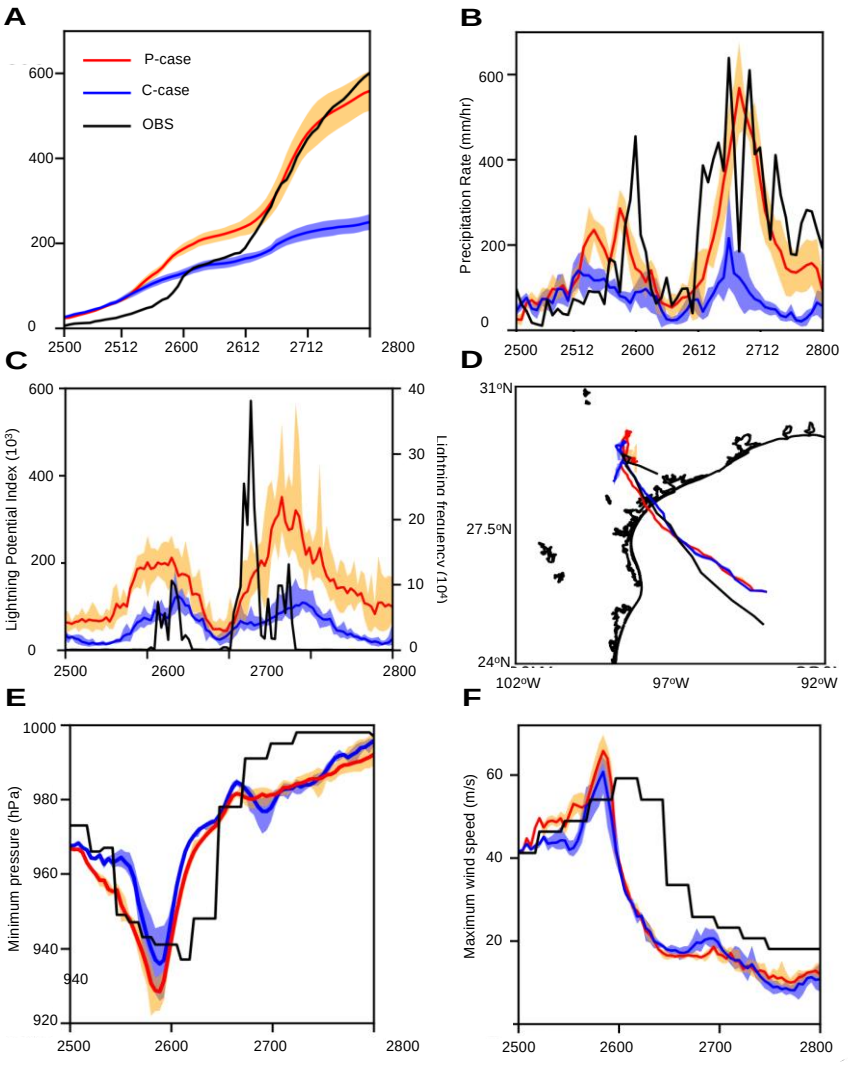

Figure 3. Aerosol effects on hurricane evolution. (a and b) Temporal evolution of the accumulative precipitation (a, mm) and precipitation rate (b, mm hr^{-1}) in the Houston urban area, showing two intense precipitation periods, i.e., during 1000 UTC – 1300 UTC 26 August (Rain I) and 0000 – 1800 UTC 27 August (Rain II). The black curve corresponds to the measurements, and the blue and red curves denote the simulations in the C- and P-Cases, respectively. (c) Temporal evolutions in simulated LPI (Right axis) in C- (blue) and P-Case (red) and observed lightning frequency (left axis) by HLMA from 0000 UTC 26 August to 2330 UTC 27 August and in the southeast Texas region. (d) Comparison of the storm tracks between the observation and simulation in the C- (blue) and P-Case (red). (e and f) Comparison of the minimum pressure (e, mb) and maximum wind speed (f, m s^{-1}) between the observation and simulation in the C- (blue) and P-Case (red). The x-axis is labeled as DDHH, i.e., 2500 for 0000 UTC 25 August. The results from a to b are averaged over the Houston urban area (Figure S3B). The shaded area in a to d, e, and f denotes the range of deviation from the ensemble simulations.

©2020 American Geophysical Union. All rights reserved.

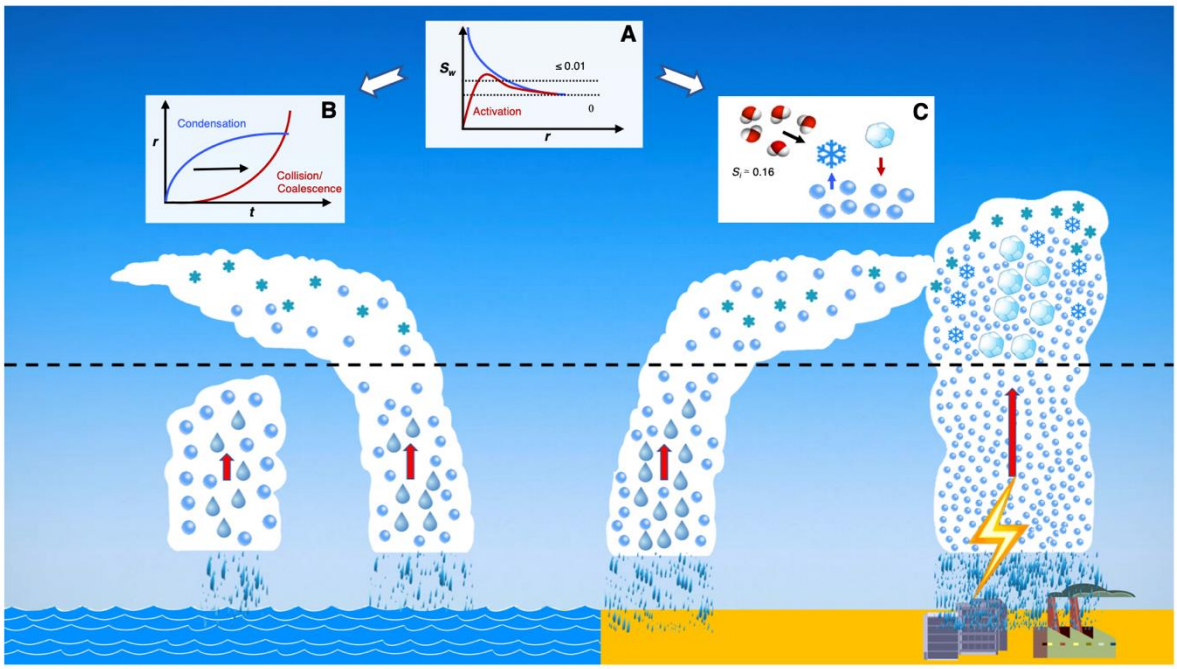

Figure 4. Mechanism of industrialization-exacerbated precipitation and lighting, including (a) aerosol activation as CCN, (b) warm rain processes, and (c) mixed-phase processes. The aerosol-hindered warm precipitation is explained by the formation of high concentrations of size-uniform small cloud droplets, which inhibit collision/coalescence. In the absence of warm precipitation, cloud droplets are effectively transported above the freezing level to promote the growth of ice hydrometeors by deposition and riming, leading to enhanced latent heat release and large ice hydrometeors. Also, the co-existence between supercooled droplets and ice hydrometeors (snowflakes and graupels) is essential for cloud electrification.

Accepted

©2020 American Geophysical Union. All rights reserved.